Terahertz resonance switch induced by the polarization conversion of liquid crystal in compound metasurface

Article *in* Optics Letters · May 2019

DOI: 10.1364/OL.44.002450

5 authors, including:

Shi-Tong Xu
Qufu Normal University
17 PUBLICATIONS **125** CITATIONS
SEE PROFILE

Fei Fan
Nankai University
91 PUBLICATIONS **907** CITATIONS
SEE PROFILE

Optics Letters

Terahertz resonance switch induced by the polarization conversion of liquid crystal in compound metasurface

Shi-Tong Xu,[1] Fei Fan,[1,3,*] Yun-Yun Ji,[1] Jie-Rong Cheng,[1] and Sheng-Jiang Chang[1,2,4]

[1]Institute of Modern Optics, Nankai University, Tianjin 300350, China
[2]Tianjin Key Laboratory of Optoelectronic Sensor and Sensing Network Technology, Tianjin 300350, China
[3]State Key Laboratory of Applied Optics, Changchun Institute of Optics, Fine Mechanics and Physics, Chinese Academy of Sciences, Changchun 130033, China
[4]e-mail: sjchang@nankai.edu.cn
*Corresponding author: fanfei_gdz@126.com

Received 11 April 2019; accepted 17 April 2019; posted 18 April 2019 (Doc. ID 364885); published 9 May 2019

We experimentally demonstrate an active terahertz (THz) resonance switch induced by the polarization conversion in a compound metasurface, which is a LC layer sandwiched by a metallic wire grating and resonance metamaterial (LCGM). Here, the liquid crystal (LC) plays the role of polarization conversion, which can induce the TE resonance. Moreover, there exists a localized resonance between metallic grating and metamaterial layers, and then the excited resonance will be greatly enhanced. The results show that the high extinction ratio of the resonance switch exceeds 30 dB at 0.82 THz. This work will bring new ideas for the research in developing THz phase, polarization, and switch devices with LC and metasurface.

https://doi.org/10.1364/OL.44.002450

Terahertz (THz) is the electromagnetic wave between the 0.1 and 10 THz band, which belongs to the cross field of photonics and electronics [1]. This unique position of the spectrum determines that it has the superiority in imaging, spectroscopy, and communication [2–4]. To realize these applications, THz functional devices are indispensable. Liquid crystals (LC) possess the optical anisotropy and high controllability under external temperature [5], optical field [6], and electric and magnetic fields [7,8], which can be used to fabricate the THz functional devices, such as THz modulator [9], filters [10], absorber [11], switches [12], phase shifter [13], and polarization controller [14].

Metasurfaces with subwavelength elements arranged in a periodic or quasiperiodic manner have been widely investigated. The amplitude, phase, and polarization state can be controlled flexibly by designing the geometry [15–18]. The combination of these artificial microstructures and LC bring new development for active THz devices [19–22]. For example, Kowerdziej *et al.* [23] proposed a thermal-controlled THz LC metamaterial, which has 7% transmittance modulation and 6 GHz frequency tuning range from 25°C to 50°C. Chen *et al.* [24] proposed a tunable THz metamaterial based on dual-frequency LC under external electric field, which realized the frequency tuning range of 15 GHz. Shrekenhamer *et al.* [25] demonstrated all-electronic controlled LC-metamaterial absorbers, which achieved 30% amplitude tuning of the absorption and 4% frequency tunability. Kowerdziej *et al.* [26] presented a tunable THz metamaterial embedded in LC, which has a maximum intensity modulation of 22% under the high voltage of 200 V. However, the resonance modulation or frequency shift of these devices is mainly dependent on the limited tunable range of LC refractive index by an external field, which leads to the problems of a strong external field, small tuning range, and low modulation depth in these THz LC devices.

In this Letter, we demonstrate an electrically controlled compound metasurface for THz resonance switch with a LC layer sandwiched by metallic wire grating and resonance metamaterial (LCGM) under the preanchoring of the external magnetic field. Different from traditional LC infiltrated metasurface, the LC layer plays the role of polarization conversion for as a tunable birefringence crystal in this LCGM, which actively induces the TE resonance mode excited or disappeared. Moreover, due to the localized resonance and multireflections of THz waves between two metallic layers, this resonance can be enhanced, which leads to a high modulation depth and a low bias voltage.

The structure of the LCGM is shown in Fig. 1(a). A 5 CB LC layer of 800 μm thickness is sandwiched between the metallic subwavelength wire grating and a resonance metamaterial. The resonance metamaterial and grating are both fabricated by conventional photolithography with 200 nm thickness gold film on 500-μm-thick fused silica [27], of which detailed structures are shown in Fig. 2. A thin graphite layer is on the surface of resonance metamaterial as the back electrode, which is formed by the natural drying of the graphene solution (G139799, Aladdin Industrial Co., Ltd.). The upper electrode is deposited on the metallic grating. When a DC bias is applied on these two electrodes, a variable electric field (E field) can be

applied along the z axis. Here, the electric field intensity of 1 KV/m corresponds to biased voltage of 0.8 V. In addition, a pair of permanent magnets apply a static magnetic field (M field), which preanchors LC molecules along the y axis. The M field $B = 0.17T$ is constant.

When $0 < E < 6$ KV/m, the M field is large enough that the LC molecules are arranged strictly along the y axis, as shown in Fig. 1(a). When $6 < E < 20$ KV/m as shown in Fig. 1(b), LC molecules start to rotate to the z axis, are in an intermediate state, and have an angle to the y axis. When the E field is strong enough ($E \geq 20$ KV/m), the LC molecules will approximately reside along the z axis. In fact, in this 1 mm thick LC cell, the low voltages of ≤16 V cannot perfectly reorient LC molecules along the z axis. The farther into the cell, the reorientation of LC molecules decreases, but it does not affect the basic function of the device. If the E field is removed, LC molecules will turn along the y axis under the force of the M field. Therefore, the optical axis of the LC can be actively rotated in the y–z plane controlled by the intensity of the E field.

A standard THz time-domain spectroscopy (THz-TDS) system was used to demonstrate experimental measurements. The THz pulse was generated by a low-temperature grown GaAs photoconductive antenna. The excitation source was a Ti:sapphire laser with 75 fs duration of 80 MHz repetition rate at 800 nm. A ZnTe crystal was used for detection. All the experiments were carried out at room temperature with humidity less than 5% [28]. The transmission and phase spectra can be both obtained by Fourier transform of the measured time-domain signals.

We tested the discrete components of the composite devices by the THz-TDS. First, the graphite layer has a high intensity transmission of nearly 90% as shown in Fig. 2(a). Second, a resistivity of 20 KΩ·cm is measured, so the graphite layer can be regarded as a transparent electrode for THz waves. In addition, the surface morphology of graphite was measured by profilometer, as shown in Fig. 2(a). The thickness of the graphite layer is about 2.42 μm, and the surface has a little fluctuation within 1 μm. Figure 2(b) shows the transmission spectrum of the metallic grating. The grating constant is 20 μm, and the duty ratio is 0.5. 0° and 90° in this figure represent

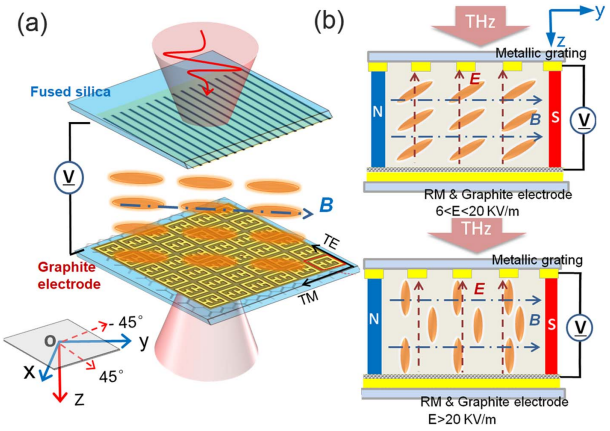

Fig. 1. (a) Schematic diagram of compound metasurface LCGM under the tunable biased electric field and static magnetic field. (b) A sectional view of LC molecular orientation in LCGM when 6 KV/m < E < 20 KV/m and E > 20 KV/m.

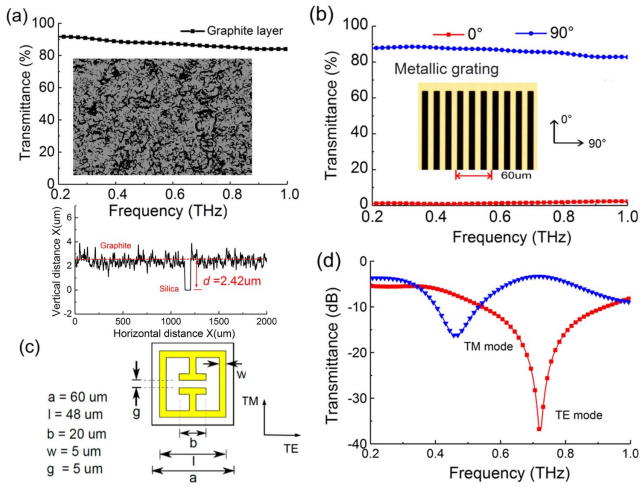

Fig. 2. (a) Transmission spectrum for the surface morphology of the graphite layer on the silica. Inset: microscope image. (b) Transmission spectrum and microscope image of the metallic grating. (c) The geometries of the metamaterial. (d) Transmission spectra of single metamaterial for TM and TE polarizations.

the polarizations that are parallel and perpendicular to the metallic wire, respectively. When the polarization state is 0°, the light is almost totally reflected by the metallic wire grating. When the polarization state is 90°, the THz waves have a high transmittance of 90%, and the remaining 10% comes from the surface reflection and transmission loss of the silica. Therefore, the metallic grating can be used as a good linear polarizer in the THz band. Figure 2(d) shows the transmission spectrum of single metamaterial, and their structural parameters are shown in Fig. 2(c). We can see that the metamaterial has two distinct resonances in TM and TE polarization directions. The resonance valleys are located at 0.46 and 0.71 THz, of which transmittances are −16.3 and −36.5 dB, respectively. Therefore, the resonances of metamaterial are strongly dependent on the two orthogonal polarization modes.

Next, we focus on the composite devices of the LCGM. As shown in Fig. 1(a), the orientation of the grating layer and resonance metamaterial layer is arranged as an angle of 45° to the y axis, and the wire of the grating is parallel to the gap of resonance metamaterial. Here the M field is always applied along the y axis, and then the initial orientation of LC is along the y axis. Due to this unique configuration, the polarization of input THz waves that pass through the metallic grating is along the −45° direction and it has a 45° angle with the optical axis of LC. Therefore, some of the wave components will be converted into the orthogonal polarization state due to the polarization conversion of LC. As a result, the output waves from the metamaterial will carry both TM and TE resonance modes when the E field is lower than the threshold of 6 KV/m. With the increase of the E field, the LC molecules rotate to the z axis in the y–z plane because the propagation direction of THz waves is parallel to the main optical axis of LC, then the LC layer gradually loses the ability of the polarization conversion. When the orientation of LC is approximately along the z axis, the out polarization that passes through the LC layer is still along the direction of −45°, so only the TM resonance mode can be excited by the resonance metamaterial.

Figure 3(a) shows that the main pulses from 4 to 6.5 ps have little shift and from 6.5 to 8.5 ps move forward as the E field increases. Importantly, the following is a deputy pulse from 10 to 12 ps, and its amplitude drops down with the increase of the E field. The corresponding transmittance spectra are shown in Fig. 3(b). There is a resonance at the low frequency of about 0.35 THz, and it has a small blue shift to 0.4 THz with the increase of the E field. And there is a larger resonance (−45 dB) at a high frequency of 0.82 THz when $E = 0$, and the resonance depth decreases with the increase of the E field, and the resonance finally disappears (14 dB) when $E = 20$ KV/m. This indicates the second resonance at 0.82 THz is contributed by the deputy pulse. Therefore, we realized the resonant switch by controlling the LC molecular orientation under a different E field, of which the extinction ratio exceeds 30 dB at 0.82 THz.

In addition, we also obtained the phase shift spectra by the Fourier transform of time-domain signals as shown in Fig. 3(c), and the air signal is the reference to the phase shift of samples. The overall trend of the phase shift increases linearly with the frequency, but there are two phase mutations in the range of the resonance band. The phase mutation at 0.82 THz decreases with the increase of the E field, and it disappears when $E = 20$ KV/m, the maximum phase change is 0.6π from 0 to 20 KV/m, as shown in the inset of Fig. 3(c). The variation of the phase spectra with E field is consistent with the transmittance spectra in Fig. 3(b), which reflects the same evolution of the resonance.

Compared with the TM and TE resonances of discrete metamaterial in Fig. 2(d), we conclude that the resonance in LCGM at low frequency comes from the original TM resonance of the metamaterial, while the second one at 0.82 THz is the induced TE resonance that profits from the polarization conversion of the LC. The mechanism of polarization state conversion and its induced resonance in LCGM is illustrated in Fig. 4. A localized resonance and multireflections of THz waves occur between these two layers in LCGM. The original incident polarization is the TM wave for the resonance for metamaterial. Some TM waves are transformed into TE polarization

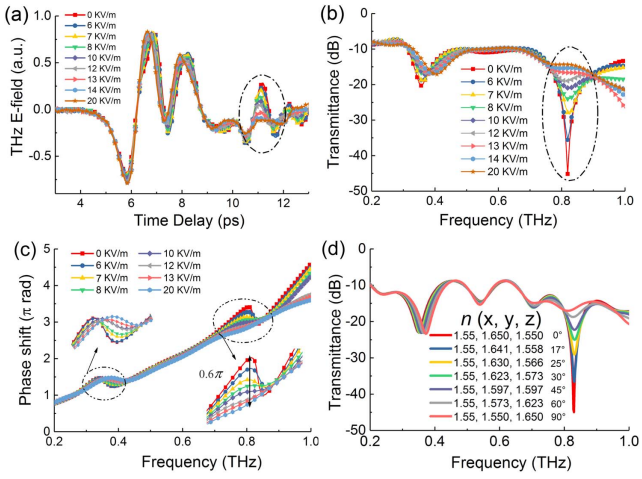

Fig. 3. (a) Experimental time-domain signals of LCGM under different E fields from 0 to 20 KV/m. (b) Transmission spectra of LCGM in dB. (c) Phase-shift spectra of LCGM. (d) Simulative transmittance spectrum of LC molecular with the different orientation angles (that is related to the refractive index in the x, y, z axes).

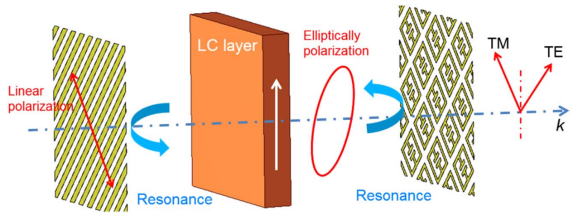

Fig. 4. Schematic diagram of polarization state conversion and resonance principle in the LCGM.

components through the LC layer and output from the back metamaterial layer. The remaining reflected waves continue to propagate in the device, and after one cycle, new TE components are generated and output. After several cycles, the total polarization conversion rates are enhanced even far away from the π phase shift point. On the back metamaterial, the total TE resonance at 0.82 THz is also enhanced with the process of multicircle polarization conversion. The higher modulation depth of LCMG originates from the polarization conversion of the LC layer and the resonance enhancement between the front and back layer, not merely from the refractive index change of LC. Therefore, this mechanism greatly enhances resonance and tunability of THz LC device [29].

The simulation is realized by using the CST software. The silica is set to be lossless with its permittivity of 3.61. Nonlinear meshes are used here with its minimum size of 1 μm. Two pairs of the periodic boundary condition are set at both x and y directions. The refractive indexes of $n_o = 1.55$ (short-axis) and $n_e = 1.65$ (long axis) are measured by the THz-TDS. We can simulate the rotation process of LC molecules under external E field by properly selecting the refractive index ellipsoid in the x, y, and z axes. In this simulation, $n_x =$ constant of $n_o = 1.55$, n_y decreases and n_z increases with the rotation of LC long axis from y to the z axis. Here, the refractive index ellipsoid of $n_{x,y,z}(1.55, 1.65, 1.55)$ means the LC molecules are arranged along the y axis (i.e., $E = 0$), whereas the refractive index ellipsoid of $n_{x,y,z}(1.55, 1.55, 1.65)$ indicates the LC molecules are arranged along the z axis (i.e., $E = 20$ KV/m). The intermediate state of the LC layer can be described by a refractive index ellipsoid, which is as follows [30]:

$$\begin{aligned} n_x &= n_o \\ n_y(\theta) &= n_o n_e / \sqrt{n_o^2 \cos^2\theta + n_e^2 \sin^2\theta} \\ n_z(\theta) &= n_o n_e / \sqrt{n_o^2 \sin^2\theta + n_e^2 \cos^2\theta}, \end{aligned} \tag{1}$$

where the orientation angle of LC is between the optical axis of LCs, and the y axis is defined as θ, n_y, and n_z are the refractive indices of the x components and y components, which can be calculated by the different value of θ. Therefore, we simulate the transmission spectra shown in Fig. 3(d), which has a good agreement in resonance positions and depths with the experimental results. The small fluctuations from 0.4 to 1.82 THz in the simulation originate from the deviation in CST simulation, which cannot perfectly reappear in the practical structure.

Furthermore, we demonstrate the induced current distributions of LCGM under different refractive index at the second resonance of $f = 0.82$ THz. The current distribution of 45 dB resonance dip with $n_{x,y,z}(1.55, 1.65, 1.55)$ is shown in Fig. 5(a), in which the currents are oscillating strongly along

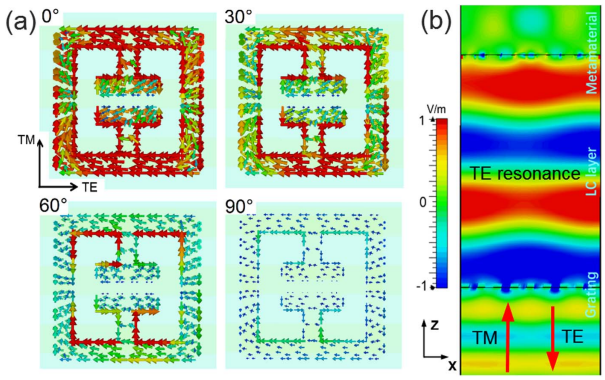

Fig. 5. (a) Simulative current distribution of LCGM at 0.82 THz with different LC orientation angles under certain E fields. (b) Simulative TE field distribution of LCGM when $\theta = 0°$ at 0.82 THz in the x–z cutting plane.

the upper and lower metal strips. The strength of the currents oscillating gradually decreases from 0 to 90°, and it matches well with the variation of the resonance depth in Fig. 3(d). The direction of the current oscillation also indicates that the resonance is excited by the TE polarization. In addition, Fig. 5(b) shows the TE field distribution of LCGM, and the input TM waves cannot be seen in the x–z cutting plane. The intermediate LC layer can be regarded as a Fabry–Perot like microcavity between the metallic grating layer and metamaterial layer. Under the multireflection and polarization conversation of the microcavity, the input TM polarization was transformed into the TE polarization, and most of them are localized in the LC layer and then reflect back. Therefore, there is almost no TE polarization component that can output from LCGM, and a large resonance dip is formed at 0.82 THz.

In summary, the LC metasurface with metallic wire grating and resonance metamaterial has been experimentally and numerically investigated in the THz regime, which can be used as a THz resonance switch with the modulation depth of more than 30 dB at the resonance frequency of 0.82 THz. Compared with the single metamaterial, it indicates that the higher modulation depth and responsivity to the external electric field, which originates from the polarization conversion of the LC layer and the resonance enhancement between the metallic grating and metamaterial layers, not merely comes from the refractive index change of the LC layer. Therefore, this is a new mechanism that can greatly enhance the tunability of a THz LC device, which will bring new ideas for developing modulation and polarization devices with LC in the THz regime.

Funding. National Key Research and Development Program of China (2017YFA0701000); National Natural Science Foundation of China (NSFC) (61505088, 61671491, 61831012); Young Elite Scientists Sponsorship Program by Tianjin (TJSQNTJ-2017-12).

REFERENCES

1. M. Tonouchi, Nat. Photonics **1**, 97 (2007).
2. C. G. Wade, N. Šibalić, N. R. de Melo, J. M. Kondo, C. S. Adams, and K. J. Weatherill, Nat. Photonics **11**, 40 (2017).
3. C. S. Ponseca, Jr. and V. Sundström, Nanoscale **8**, 6249 (2016).
4. T. Nagatsuma, G. Ducournau, and C. C. Renaud, Nat. Photonics **10**, 371 (2016).
5. R.-P. Pan, C.-F. Hsieh, C.-L. Pan, and C.-Y. Chen, J. Appl. Phys. **103**, 093523 (2008).
6. L. Cattaneo, M. Savoini, I. Muševič, A. Kimel, and T. Rasing, Opt. Express **23**, 14010 (2015).
7. A. Komar, Z. Fang, J. Bohn, J. Sautter, M. Decker, A. Miroshnichenko, T. Pertsch, I. Brener, Y. S. Kivshar, I. Staude, and D. N. Neshev, Appl. Phys. Lett. **110**, 071109 (2017).
8. L. Yang, F. Fan, M. Chen, X. Zhang, J. Bai, and S. Chang, Opt. Mater. Express **6**, 2803 (2016).
9. M. Rahm, J.-S. Li, and W. J. Padilla, J. Infrared Millim. Terahertz Waves **34**, 1 (2013).
10. C.-Y. Chen and C.-L. Pan, Appl. Phys. Lett. **88**, 101107 (2006).
11. S. Savo, D. Shrekenhamer, and W. J. Padilla, Adv. Opt. Mater. **2**, 275 (2014).
12. O. Buchnev, N. Podoliak, M. Kaczmarek, N. I. Zheludev, and V. A. Fedotov, Adv. Opt. Mater. **3**, 595 (2015).
13. C.-S. Yang, T.-T. Tang, R.-P. Pan, P. Yu, and C.-L. Pan, Appl. Phys. Lett. **104**, 141106 (2014).
14. B. Vasić, D. C. Zografopoulos, G. Isić, R. Beccherelli, and R. Gajić, Nanotechnology **28**, 124002 (2017).
15. H.-T. Chen, W. J. Padilla, J. M. O. Zide, C. Gossard, A. J. Taylor, and R. D. Averitt, Nature **444**, 597 (2006).
16. L. Zhang, S. Mei, K. Huang, and C.-W. Qiu, Adv. Opt. Mater. **4**, 818 (2016).
17. L. Cong, P. Pitchappa, Y. Wu, L. Ke, C. Lee, N. Singh, H. Yang, and R. Singh, Adv. Opt. Mater. **5**, 1600716 (2017).
18. S. Liu, T. J. Cui, Q. Xu, D. Bao, L. Du, X. Wan, W. X. Tang, C. Ouyang, X. Y. Zhou, H. Yuan, H. F. Ma, W. X. Jiang, J. Han, W. Zhang, and Q. Cheng, Light: Sci. Appl. **5**, e16076 (2016).
19. L. Wang, X.-W. Lin, W. Hu, G.-H. Shao, P. Chen, L.-J. Liang, B.-B. Jin, P.-H. Wu, H. Qian, Y.-N. Lu, X. Liang, Z.-G. Zheng, and Y.-Q. Lu, Light: Sci. Appl. **4**, e253 (2015).
20. Z. Shen, S. Zhou, S. Ge, W. Duan, P. Chen, L. Wang, W. Hu, and Y. Lu, Opt. Lett. **43**, 4695 (2018).
21. B.-Y. Wei, S. Liu, P. Chen, S.-X. Qi, Y. Zhang, W. Hu, Y.-Q. Lu, and J.-L. Zhao, Appl. Phys. Lett. **112**, 121101 (2018).
22. Y.-Y. Ji, F. Fan, X.-H. Wang, and S.-J. Chang, Opt. Express **26**, 12852 (2018).
23. R. Kowerdziej, M. Olifierczuk, and J. Parka, Opt. Express **26**, 2443 (2018).
24. C.-C. Chen, W.-F. Chiang, M.-C. Tsai, S.-A. Jiang, T.-H. Chang, S.-H. Wang, and C.-Y. Huang, Opt. Lett. **40**, 2021 (2015).
25. D. Shrekenhamer, W.-C. Chen, and W. J. Padilla, Phys. Rev. Lett. **110**, 177403 (2013).
26. R. Kowerdziej, L. Jaroszewicz, M. Olifierczuk, and J. Parka, Appl. Phys. Lett. **106**, 092905 (2015).
27. S.-T. Xu, F. Fan, M. Chen, Y.-Y. Ji, and S.-J. Chang, Appl. Phys. Lett. **111**, 031107 (2017).
28. J.-P. Yu, S. Chen, F. Fan, J.-R. Cheng, S.-T. Xu, X.-H. Wang, and S.-J. Chang, Opt. Express **26**, 663 (2018).
29. S.-T. Xu, S. Chen, L. L. Mou, F. Fan, Z. F. Liu, and S. J. Chang, Carbon **139**, 801 (2018).
30. I. C. Khoo, D. H. Werner, X. Liang, A. Diaz, and B. Weiner, Opt. Lett. **31**, 2592 (2006).